

Near Infrared Observations at 1.56 μm of the 2003 October 29 X10 White-Light Flare

Yan Xu¹, Wenda Cao^{1,2}, Chang Liu¹, Guo Yang¹, Jiong, Qiu^{1,2}, Ju Jing¹
Carsten Denker^{1,2} and Haimin Wang^{1,2}

1. *Center for Solar-Terrestrial Research, New Jersey Institute of Technology
323 Martin Luther King Blvd, Newark, NJ 07102*

2. *Big Bear Solar Observatory, 40386 North Shore Lane, Big Bear City, CA 92314*

yx2@njit.edu

ABSTRACT

We present high resolution observations of an X10 white-light flare in solar active region NOAA 10486 obtained with the Dunn Solar Telescope (DST) at the National Solar Observatory/Sacramento Peak (NSO/SP) on 2003 October 29. Our investigation focusses on flare dynamics observed in the near-infrared (NIR) continuum at 1.56 μm . This is the first report of a white-light flare observed in the NIR. The spatial resolution was close to the diffraction limit of the 76 cm aperture DST. The data benefited from a newly developed high order adaptive optics (AO) system and a state-of-the-art NIR complex metal oxide semiconductor (CMOS) focal plane array (FPA). In addition, we compared hard X-ray (HXR) data of the Ramaty High Energy Solar Spectroscopic Imager (RHESSI) and magnetograms of the Michelson Doppler Imager (MDI) onboard the Solar and Heliospheric Observatory (SoHO) with the NIR continuum images. Since the NIR data were observed at the opacity minimum, only the most energetic electrons can penetrate to this layer in the deep photosphere. As a consequence, the flare ribbons appear to be very thin ($< 2''$) and well defined. During the impulsive phase of the flare, two major flare ribbons moved apart, which were both temporally and spatially correlated with RHESSI HXR ribbons. The ranges of two ribbons are 18% to 25% brighter than the quiet sun NIR continuum. The separation speed of the ribbons is about 38 km/s in regions with weak magnetic fields and decreases to about 19 km/s, where stronger magnetic fields are encountered. The derived electric field in reconnection current sheet E_c is of order 45 V cm^{-1} at the flare maximum.

Subject headings: Sun: activity – Sun: flares – Sun: infrared – Sun: photosphere

1. Introduction

Flares are generally regarded as the results of sudden magnetic energy release in the solar corona. Charged particles are created and accelerated. Some are non-thermal electrons that loose their energy in the lower atmosphere (chromosphere) by emitting HXR through a bremsstrahlung process and microwave radiation through a gyro-synchrotron process (Brown 1971; Emslie 1978). Among all flares, the most energetic flares are white-light flares or “photospheric flares” (Najita and Orrall 1970). They always require a larger high energy particle flux and less relaxation time than ordinary flares (Neidig

1989). According to the standard flare model, the white-light continuum emission is caused by precipitation of non-thermal electrons to chromosphere and photosphere (Asai et al. 2002). Localized heating and ionization due to the non-thermal electrons can produce an enhancement of continuum brightness. Observations of white-light flares in the visible continuum have been reported by a number of authors (Canfield et al. 1984; Canfield and Gayley 1987; Hawley and Fisher 1994). Furthermore, Ohki and Hudson (1975) predicted almost 30 years ago, that accelerated particles can even propagate to the lower photosphere and can be detected in NIR continuum images. However, an observational proof of NIR white-light flare has not been presented, yet.

The observations at $1.56 \mu\text{m}$ presented in this letter combine high cadence with high-spatial resolution. Since the solar opacity minimum is at about $1.6 \mu\text{m}$, we can probe the deepest layer of solar photosphere, which is about half a scale-heights deeper than the visible continuum (Wang et al. 1998). NIR observations give us an access to the height dependence of electron precipitation and valuable clues to study flare energetics. The improved seeing in the NIR, which is proportional to $\lambda^{6/5}$ and about four times better than at 500 nm , but comes with the cost of lower feature contrasts and lower spatial resolution compared to visible-light observations. Nonetheless, the improved signal-to-noise ratio achieved with the AO system and a spatial resolution of about $0.45''$ alleviates these limitations. Another cornerstone of this NIR observations is a newly acquired by CMOS FPA manufactured by Rockwell Scientific Imaging that has been temporarily moved from BBSO to the DST to work in tandem with the AO system. In the following sections, we present the first NIR continuum flare observations based on these novel instruments and detectors illustrating morphology, proper motions, and evolution of flare ribbons.

2. Observations and Data Reduction

The X10 flare was observed in solar active region NOAA 10486 on 2003 October 29. NOAA 10486 was one of the surprises in the declining phase of solar cycle No. 23 and produced several major flares including an X17.2 flare on the previous day and an X28 flare on 2003 November 4, which was the largest X-ray flare in the recorded history.

The BBSO NIR CMOS FPA is based on a TCM8600 read-out integrated circuit (ROIC). The same type of HgCdTe/ Al_2O_3 technology is commonly used in night-time astronomy. However, this ROIC has been designed for shorter exposure times and faster data acquisition rates encountered in solar applications. A liquid nitrogen cooling system is required to minimize the dark signal and prevent self-illumination of the ROIC. The characteristics of the 1024×1024 pixel detector are a quantum efficiency better than 60%, a dynamic range better than 70 dB, a 14-bit digitization depth, and a 30 frames per second data acquisition rate. In addition to novel detector technology, we used the newly developed high-order AO system at the DST (Rimmele 2000; Rimmele et al. 2003). The field-of-view (FOV) was $91'' \times 91''$ resulting in an image scale of $0.089''$ per pixel. The diffraction limit at $1.56 \mu\text{m}$ is $\theta = \lambda/D = 0.42''$, where D is the telescope aperture. Therefore, our data is oversampling by about 2.3 times of the diffraction and gives more reliable information. The exposure time was 13 ms which is sufficient short to freeze the seeing in the NIR, because the longest exposure time for freezing wavefront aberrations is about 40 ms in the visible band (Denker et al. 2004) and about 150 ms in NIR according to the $\lambda^{6/5}$ law. The bandpass was restricted by a 5 nm custom made interference filter. Although there are few Fraunhofer lines within this 5 nm range, but they only contribute less than 2% of all the radiation goes through the filter. Therefore, we can use this data as continuum. All NIR images are dark and flat field corrected. Every minute, we selected the best frame with the highest granular

contrast out of a total of 50 frames. Image motion and differential image motion were removed from the final 1-minute cadence time sequence.

In addition, the AO corrected data were also acquired in visible channel simultaneously with NIR channel. The observations were taken by a 1024×1024 pixel 1 M15 12-bit CCD camera manufactured by Dalsa in green continuum centered at 520 nm and the bandpass was 52 nm. We used 4 ms short-exposure and took 100 frames selected from 200 frames every minutes in order to do the speckle masking reconstruction. The FOV of these speckle interferometry channel was $81'' \times 81''$ and centered with the NIR channel. After frame selection, speckle masking technique has been applied. The details and results of speckled images will be presented in a separate paper (Denker et al. 2004).

Figure 1 shows the high quality IR image with flare kernels taken on 20:42 UT and a speckled visible image illustrating the improvement of image quality taken on 16:48 UT. Figure 2 shows a time sequence of NIR images with superimposed RHESSI HXR contours. In order to compare the NIR images with RHESSI HXR maps, we used the TRACE white-light data as reference images.

The MPEG movies of the full resolution NIR time sequence clearly show the flare evolution and proper motion of the flare ribbons. Unlike the RHESSI data, we can figure out two-dimensional information about the flare ribbons, marked by red dots in Figure 2 are the IR flare ribbons. In order to see the ribbons more clearly, contrast enhanced difference maps are shown in Figure 3. The first step to enhance the contrasts of NIR flare ribbons is subtracted each frame of the well aligned images sequence by a reference frame which is right before the time of the flare. Then, we applied a high-pass filter to get rid of the background. We can see that the IR ribbons are correlated with the cores of HXR contours very well, but they are much thinner.

3. Results

In Figure 1, the blue contours represent RHESSI HXR kernel, which are well correlated with NIR intensity maxima shown in red. The X10 white-light flare started at 20:39 UT and ended at 20:52 UT. The X-ray flux peaked around 20:47 UT. However, at high energies between 25 keV and 300 keV, the flare had two peaks. The first peak occurred around 20:44 UT. Unfortunately, our data did not cover the period of the second peak. The NIR data also show the maximum flare emission between 20:42 UT and 20:45 UT. The flare ribbons were initially visible around 20:40 UT, approximately at the same time when the HXR kernels appeared.

The intensity enhancement of the flare ribbons is about 18% to 25% compared to NIR quiet sun background and 28% to 45% compared to visible quiet sun background. We did not use the speckled visible data to measure the contrast, but frame selection and de-stretch procedure were applied. According to Wang et al. (1998), the intensity enhancement of a flare is given by

$$\frac{\Delta I}{I} = \frac{B(T_0 + \Delta T, \lambda) - B(T_0, \lambda)}{B(T_0, \lambda)} \quad (1)$$

while the temperature perturbation is $\Delta T \approx 1000$ K in NIR and ≈ 500 K in visible during the emission maximum, where T_0 is the photospheric temperature which equals to 7600 K at $1.56 \mu\text{m}$ and 6000 K at $0.52 \mu\text{m}$ (Vernazza et al. 1981; Mauas et al. 1990), ΔT is increment of the mean flare ribbon temperature exceed, and B is the Planck function. This temperature gradient may imply that the flare near photosphere is not iso-thermal.

Analyzing the NIR time sequence, we find very fast moving flare ribbons. Since the ribbons are thin we conclude that the cooling time has to be short, so that we can use difference images to show the evolution of the flare emission more clearly (see Figure 2). The flare emission in consecutive frames occurs in distinct regions with almost no overlap, i.e., the cooling time has to be less than 1 minute, which is the time difference between two images. After careful measurements, we found that the average speed of the two ribbons is around 38 km/s within regions of weak magnetic field and decreases to 19 km/s in regions with enhanced magnetic fields. These are typical values encountered in two-ribbon flares (e.g., Wang et al. 2003, 2004).

It is well accepted that the flare ribbons speed of motion of sweeping through the magnetic field lines corresponds to the rate of magnetic flux reconnection in the corona, where generated the reconnecting current sheet. Therefore, in a two dimensional configuration, the product of motion speed V and the normal component of the magnetic field B_n is just a measurement of the local reconnection rate. The reconnection rates in opposite polarities should be equal to each other. As showed in Figure 3, the NIR flare ribbons are located in opposite polarity areas. The speed of the ribbons travelling in weak magnetic fields is faster than in region where stronger magnetic fields are encountered. The relationship between the electric field strength E_c along the current sheet and two observables, V_t and B_n were derived and simplified by Forbes and Lin(2000) according to assumptions and approximations,

$$E_c = V_t B_n \quad (2)$$

To measure the magnetic field B_n , since the active region is close to the disk center at $\mu = \cos \theta \approx 0.9$, the MDI longitudinal magnetic field B_{\parallel} can be used as B_n . The magnetic field has absolute values about 700 Gauss of relatively weak region and 1400 Gauss of stronger region. Combined with the speeds we measured, the maximum electric field E_c in this event is about 45 V cm^{-1} during the peak of HXR and IR white-light emission. This value is much larger than most of the previously results (Jing et al 2004; Qiu et al. 2004; Wang et al. 2003, 2004). The electric fields in the current sheet must be super-Dreicer fields in which electrons can be accelerated to such a high energy causing the emission in the opacity minimum.

Asai et al.(2002) found that the areas in $\text{H}\alpha$ ribbon accompanied by HXR have a magnetic strength about three times larger than those without HXR radiation. During their event, the active region was relatively simple and those two point with higher magnetic field were much closer to two sunspots than other flare ribbon points. We also attempt to determine the relation between the HXR and magnetic fields along the flare ribbon areas, but did not find such a difference between magnetic fields inside HXR kernel and outside HXR kernel. Although we used the NIR flare ribbons which were thinner than the $\text{H}\alpha$ ribbons, but they are still longer than HXR source.

A remote ribbon is located in the upper FOV during this event. From Figure 1, we can see that, unlike other two ribbons, this ribbon had almost no HXR radiation and its white-light emission is lower. It appeared two to three minutes later than the other two ribbons and did not move for a long distance. Therefor, this remote ribbon should not be a major part of this flare but is due to electrons travelling to the remote site along large scale magnetic loops.

4. Discussion

In this letter, we report the first photometric NIR observations of a white-light flare. At $1.56 \mu\text{m}$, we were able to study properties of flare in the deepest photospheric layers. Flare kernels and ribbons

are clearly seen in NIR images of unprecedented quality, allowing us to measure ribbon brightness and separation speed.

White-light flare emission is commonly attributed to non-thermal electron beams generated at the top of flare loops heating the lower atmosphere. Previous white-light flare studies were focused on chromosphere and upper photosphere, because strong heating near the quiet Sun $\tau = 1$ level seemed to be unlikely (Neidig 1989). At this moment, no models exist encompassing a detailed explanation of the enhanced NIR emission. However, we conclude that our observations agree with the electron precipitation theory, since HXR emission and NIR intensity enhancement are well correlated.

The electric fields were derived by measuring the ribbon motion and the magnetic fields along the ribbon. We found a maximum of the electric fields of 45 V cm^{-1} , and an average value of 25 V cm^{-1} which are much higher than previous results using the same method. Since the electric fields represent the magnetic reconnection rate and the released energy accelerating electrons, we believe that in order to have a white-light flare, especially an IR flare, the electric fields must be high, e.g., large separation speed with high magnetic fields in reconnection region.

This work is supported by NSF under grants ATM-0313591, ATM- 0236945, ATM-0233931, and AST-9987366, by NASA under grants NAG5-10910, NAG5-10212, and NAG5-12733 and by NSFC-10103004, and NSF of Yunnan through 2001A0027Q. Obtaining the excellent data would not have been possible without the help of the dedicated observing staff at the Dunn Solar Telescope. The National Solar Observatory is a Division of the National Optical Astronomy Observatories, which is operated by the Association of Universities for Research in Astronomy, Inc., under cooperative agreement with the National Science Foundation.

REFERENCES

- Asai, A., Masuda, S., Yokoyama, T., Shimojo, M., Isobe, H., Kurokawa, H., & Shibata, K. 2002, *ApJ*, 578, L94
- Brown, J. 1971, *Sol. Phys.*, 18, 489
- Canfield, R. C., Gunkler, T. A., & Ricchiazzi, P. J. 1984, *ApJ*, 282, 296
- Canfield, R. C., & Gayley, K. G. 1987, *ApJ*, 422, 999
- Denker, C., Mascarinas, D., Xu, Y., Cao, W., Yang, G., Wang, H., & Goode, P. R. 2004, *Sol. Phys.*, submitted
- Ding, M. D., Fang, C., Gan, W. Q., & Okamoto, T. 1994, *ApJ*, 429, 890
- Emslie, A. J. 1978, *ApJ*, 224, 241
- Forbes, T. G. & Lin, J. 2000, *J. Atmos. Sol.-Terr. Phys.*, 62, 1499
- Hawley, S. L. & Fisher, G. H. 1994, *ApJ*, 426, 387
- Jing, J., Qiu, J., Qu, M., & Wang, H. 2004, *ApJ*, in preparation
- Mauas P. J. D., Machado, M. E., & Avrett, E. H. 1990, *ApJ*, 360, 715

- Najita, K. & Orrall, F. Q. 1970, *Sol. Phys.*, 15, 176
- Neidig, D. F. 1989, *Sol. Phys.*, 121, 261
- Ohki, K. & Hudson, H. S. 1975, *Sol. Phys.*, 43, 405
- Qiu, J., Wang, H., Cheng, C. Z., & Gary, D. E. 2004, *ApJ*, submitted
- Rimmele, T. 2000, *Proc. SPIE*, 4007, 218
- Rimmele, T. R., Richards, K., Hegwer, S. L., Ren, D., Fletcher, S., Gregory, S., Didkovsky, L. V., Denker, C., Marquette, W., Marino, J., & Goode, P. R. 2003, *Proc. SPIE*, 4839, 635
- Vernazza, J. E., Avrett, E. H., & Loeser, R. 1973, *ApJS*, 45, 635
- Wang, H., Spirock, T. J., Goode, P. R., Lee, C., Zirin, H. & Kosonocky, W. 1998, *ApJ*, 495, 964
- Wang, H., Qiu, J., Jing, J., & Zhang, H. 2003, *ApJ*, 593, 564
- Wang, H., Qiu, J., Jing, J., Spirock, T. J., Yurchyshyn, V., Abramenko, V., Ji, H., & Goode, P. R. 2004, *ApJ*, submitted

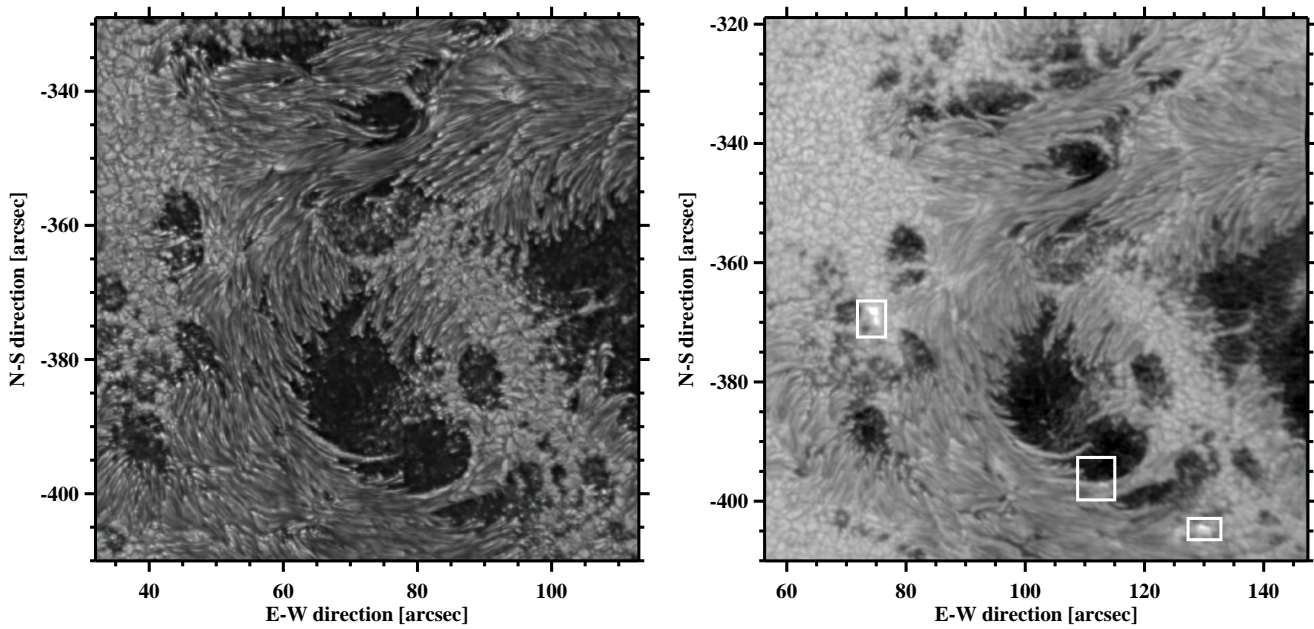


Fig. 1.— Left Panel: Reconstructed image of active region NOAA 10486 after correction of high-order, frame selection and speckle masking processing. It was observed at 16:48 UT on 2003 October 29. The FOV was $81 \times 81''$. Right Panel: NIR image of the same active region during the flare time taken on 20:42 UT with a FOV of $91 \times 91''$. The bright patches marked by white boxes are NIR flare kernels.

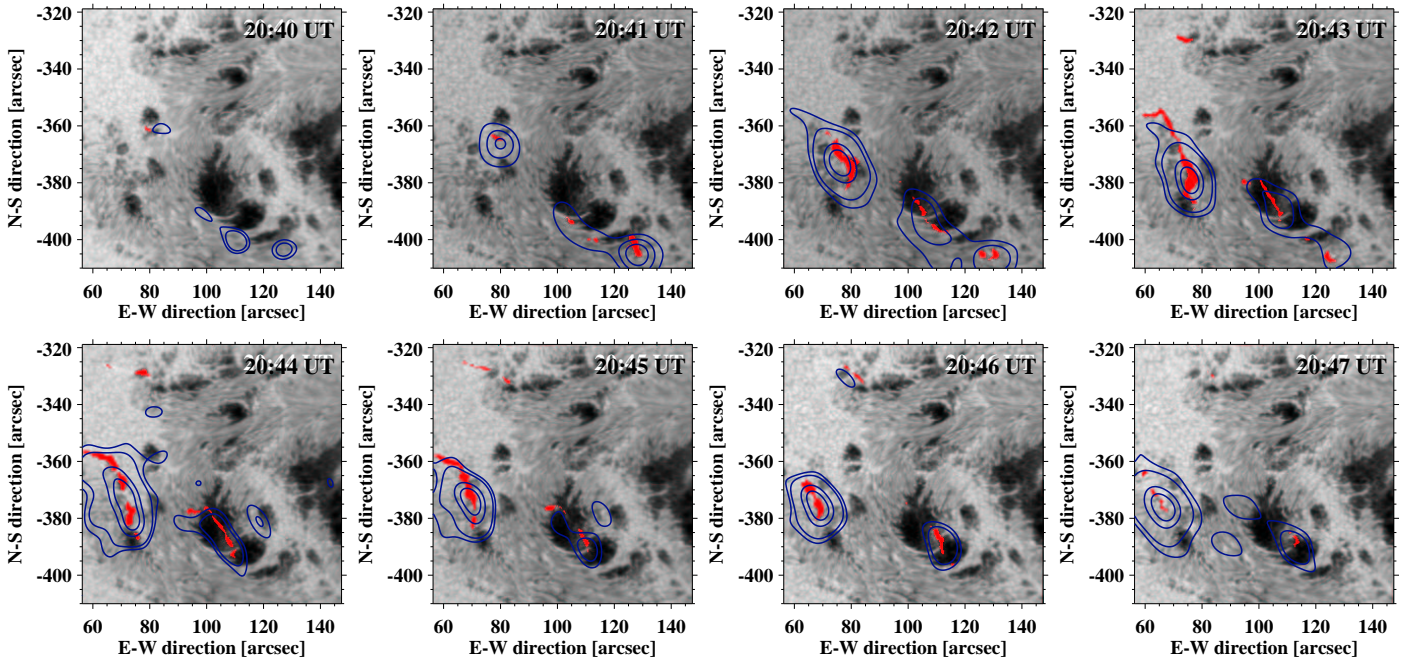


Fig. 2.— NIR time sequence images of the X10 flare from 20:40 UT to 20:47 UT on 2003 October 29. RHESSI HXR contours (blue) corresponding to the 50-100 keV channel with 60 seconds integration. The local NIR intensity maxima are shown in red. Two flare ribbons are correlated with strong HXR kernels. HXR contour levels are drawn at 0.17, 0.25, 0.60, and 0.80 of the maximum intensity, except for the first two frames, where they correspond to 0.7 and 0.8 for the first frame and 0.4, 0.6, 0.8 for the second, since the HXR kernel were weaker at that time. The annotation of the axes refers to heliographic coordinates corresponding to a FOV of $91 \times 91''$.

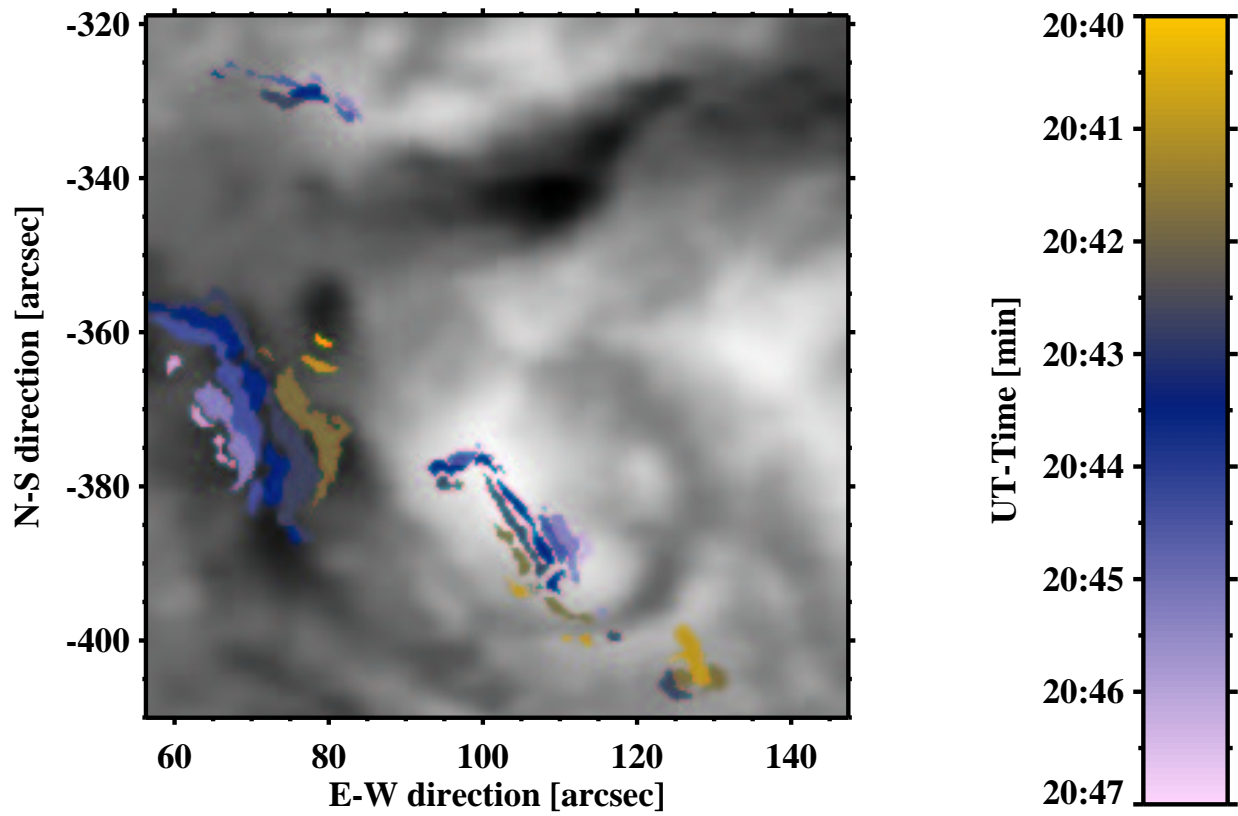


Fig. 3.— NIR difference images showing the temporal evolution of the flare ribbons from 20:40 UT to 20:47 UT. The background is an MDI line-of-sight magnetogram.